

# XMM-Newton observations of four millisecond pulsars

Vyacheslav E. Zavlin<sup>1</sup>

## ABSTRACT

I present an analysis of the XMM-Newton observations of four millisecond pulsars, J0437–4715, J2124–3358, J1024–0719, and J0034–0534. The new data provide strong evidence of thermal emission in the X-ray flux detected from the first three objects. This thermal component is best interpreted as radiation from pulsar polar caps covered with a nonmagnetic hydrogen atmosphere. A nonthermal power-law component, dominating at energies  $E \gtrsim 3$  keV, can also be present in the detected X-ray emission. For PSR J0437–4715, the timing analysis reveals that the shape and pulsed fraction of the pulsar light curves are energy dependent. This, together with the results obtained from the phase-resolved spectroscopy, supports the two-component (thermal plus nonthermal) interpretation of the pulsar’s X-ray radiation. Highly significant pulsations have been found in the X-ray flux of PSRs J2124–3358 and J1024–0719. For PSR J0034–0534, a possible X-ray counterpart of the radio pulsar has been suggested. The inferred properties of the detected thermal emission are compared with predictions of radio pulsar models.

*Subject headings:* pulsars: individual (J0437–4715, J2124–3358, J1024–0719, J0034–0534) — stars: neutron — X-rays: stars

## 1. Introduction

Of more than 1500 currently known rotation-powered (radio) pulsars<sup>2</sup>, 122 possess very short spin periods  $P < 10$  ms. These millisecond pulsars are generally believed to be very old neutron stars (NSs), spun up by accretion in binary systems, with characteristic ages  $\tau = P/2\dot{P} \sim 0.1\text{--}10$  Gyr and low surface magnetic fields  $B_{\text{surf}} \propto (P\dot{P})^{1/2} \sim 10^8\text{--}10^{10}$  G (e.g., Taylor et al. 1993). As millisecond pulsars are intrinsically faint at optical wavelengths and most of them reside in binary systems with optically brighter white dwarf companions,

---

<sup>1</sup>Space Science Laboratory, NASA MSFC SD50, Huntsville, AL 35805; vyacheslav.zavlin@msfc.nasa.gov

<sup>2</sup>According to the catalog provided by the Australia Telescope National Facility (ATNF), <http://www.atnf.csiro.au/research/pulsar>, for the middle of 2005.

X-ray energy range is the main source of information on these objects outside the radio band. So far firm X-ray detections have been reported for nine millisecond (non-variable) pulsars, either solitary or in binaries without interaction with companions. They are given in Table 1 (this list does not include X-ray emitting millisecond pulsars in the global clusters 47 Tuc and NGC 6397 because of a lack of a detailed information on their X-ray properties — see, e.g., Grindlay et al. 2002).

X-ray emission from radio pulsars consists of two different components, thermal and nonthermal (see, e.g., Pavlov et al. 2002, and Kaspi et al. 2006 for reviews). The nonthermal component is described by a power-law (PL) spectral model and attributed to radiation emitted from pulsar magnetosphere, whereas the thermal emission can originate from either the whole surface of a cooling NS or small hot spots around the magnetic poles (polar caps; PCs) on the star surface, or both. As predicted by virtually all pulsar models, these PCs can be heated up to X-ray temperatures ( $\sim 1$  MK) by relativistic particles generated in pulsar acceleration zones. In the case of millisecond pulsars, the entire surface at a NS age of  $\sim 1$  Gyr is too cold,  $\lesssim 0.1$  MK, to be detectable in X-rays (although it may be seen in *UV/FUV* — see §2). Therefore, only nonthermal and/or thermal PC radiation is expected to be observed in X-rays from these objects. The pulsars presented in Table 1 can be divided in two distinct groups (see also Kuiper & Hermsen 2004). The first group consists of PSRs B1937+21, B1957+20, J0218+4232, and B1821–24, with high rotational energy losses,  $\dot{E} > 10^{35}$  erg s $^{-1}$ , and estimated X-ray luminosities,  $L_X \gtrsim 10^{32}$  erg s $^{-1}$ . Their X-ray emission is of a nonthermal origin, with pure PL spectra of photon index  $\Gamma = 1.5$ –2 and pulsed profiles with strong narrow peaks and large pulsed fractions,  $f_p \gtrsim 50\%$  (see references in Table 1). Probably, PSR J0751+1807 can also be associated with this group because its spectrum is better fitted with a PL model of  $\Gamma \approx 1.6$ . Three other pulsars, J0437–4715, J0030+0451 and J2124–3358, with lower spin-down energies,  $\dot{E} < 10^{34}$  erg s $^{-1}$ , belong to the second group. X-ray emission from these NSs shows significant contribution of a thermal component, with smoother pulsations and lower pulsed fractions. The properties of X-rays detected from PSR J1012+5307 are rather uncertain. However, there is an indication of a thermal component in its X-ray flux. Current theoretical models are not elaborate enough to predict in which millisecond pulsars the thermal PC component would prevail over the nonthermal one. It, however, seems certain that both the thermal and nonthermal luminosities should increase with rotational energy loss  $\dot{E}$ . Therefore, only analysis of X-ray observations can help in elucidating the radiative properties of millisecond pulsars.

The high sensitivity and spectral resolution of *Chandra* and *XMM-Newton* provide new opportunities for studying X-ray emission from faint celestial objects. This paper presents an analysis and interpretation of new *XMM-Newton* observations of four millisecond pulsars, J0437–4715, J2124–3358, J1024–0719, and J0034–0534 (§§2–5). The obtained results are

summarized and discussed in §6.

## 2. PSR J0437–4715

This is the nearest and X-ray brightest millisecond pulsar known. It is in a 5.7 d binary orbit with a low-mass white dwarf companion. Its pulsed X-ray emission was first detected with *ROSAT* in the 0.1–2 keV range (Becker & Trümper 1993). Those data could be fitted with either a single PL model of  $\Gamma \approx 2.5$ , suggesting a nonthermal origin of the detected emission, or a thermal PC model consisting of two opposite PCs covered with nonmagnetic hydrogen atmosphere<sup>3</sup> and temperature decreasing from  $\sim 1.5$  MK in the PC ”core” of about  $\sim 0.3$  km radius to  $\sim 0.4$  MK in the PC ”rim” of a  $\sim 3$  km radius (Zavlin & Pavlov 1998). Becker & Trümper (1993) found that pulsed fraction  $f_p$  of the pulsar flux increases with photon energy  $E$  from about 30% at  $E \sim 0.2$  keV up to about 50% at 1 keV (although Becker & Trümper 1999 found no energy dependence of  $f_p$  from a later *ROSAT* observation of PSR J0437–4715). On the other hand, thermal emission from NS atmospheres is essentially anisotropic, even at low  $B_{\text{surf}}$ , with radiation intensities beamed stronger at higher  $E$  (Zavlin et al. 1996), that can result in an increase of  $f_p$  with photon energy. Therefore, if the energy dependence of  $f_p$  found by Becker & Trümper (1993) is real, it could be regarded as an additional indication of the thermal origin of the detected radiation. The pulsar was also observed with *Chandra*. Analysis of the combined *ROSAT* and *Chandra* data (Zavlin et al. 2002) showed that the 0.1–7 keV spectrum of PSR J0437–4715 cannot be described with a simple one-component model and requires two components: a nonthermal PL spectrum of  $\Gamma \approx 2.0$  and a thermal PC model similar to that suggested by Zavlin & Pavlov (1998) from the *ROSAT* data alone. The thermal (bolometric) and nonthermal (in 0.2–10 keV) luminosities were found to be  $L_{\text{bol}} \approx 2.3 \times 10^{30}$  erg s<sup>−1</sup> and  $L^{\text{nonth}} \approx 0.6 \times 10^{30}$  erg s<sup>−1</sup> (for a distance  $d = 0.14$  kpc — see Table 1), respectively. In this interpretation, the nonthermal component dominates at energies  $E \gtrsim 3$  keV. The *Chandra* data provided also an energy-integrated pulse profile with  $f_p \approx 40\%$  and the X-ray peak at the same phase as the radio peak. In addition, PSR J0437–4715 is the only millisecond pulsar detected near the optical, at the wavelengths  $\lambda = 1155\text{--}1702$  (Kargaltsev et al. 2004), that provided an estimate on the temperature of the entire NS surface,  $T_{\text{surf}} \approx 0.1$  MK — surprisingly high for such an old NS, implying special heating mechanism(s) to operate in this pulsar.

---

<sup>3</sup>See Zavlin & Pavlov (2002) for a recent review on NS atmosphere models.

## 2.1. XMM-Newton observation

PSR J0437–4715 was observed with XMM-Newton on 2002 October 9 (orbit 519) for 68.3 and 67.2 ks effective exposures with the EPIC<sup>4</sup>-MOS and EPIC-pn instruments, respectively. EPIC-MOS1 and MOS2 were operated in Full Frame mode providing an image of an area of a  $\sim 14'$  radius and a time resolution of 2.6 s. EPIC-pn was in Timing mode. In this mode only one EPIC-pn CCD is in use and the EPIC-pn image is collapsed in one-dimensional (1-D) count distribution in the direction perpendicular to the CCD read-out, that provides a 0.03 ms time resolution suitable for detecting pulsations in X-ray flux of millisecond pulsars. Thin filters were used for each EPIC instrument. The EPIC data were processed with the most recent SAS package<sup>5</sup> (ver. 6.1.0).

Figure 1 presents a  $20' \times 20'$  image constructed from combined EPIC-MOS1 and MOS2 data. PSR J0437–4715 is the second brightest source in the field of view. The EPIC-pn field of view is also shown in Figure 1, as well as the direction of the CCD read-out. It is evident that the satellite position angle ( $138.7^\circ$ ) chosen for observing PSR J0437–4715 was not optimal, which led to a partial contamination of the pulsar data in the 1-D EPIC-pn image by the much brighter neighboring AGN. This resulted in an asymmetric shape of the 1-D distribution of EPIC-pn counts shown in the upper panel of Figure 2. To evaluate the contamination, we constructed three 1-D images from the EPIC-MOS data confined within the EPIC-pn field of view with the same column width of  $4''.2$  as in the EPIC-pn CCD: from the areas above and below the short-dashed line in Figure 1, which contain negligible fractions of pulsar and AGN quanta (respectively), and from the total area. Examination of these three distributions plotted in the lower panel of Figure 2 shows that the contamination of the pulsar is insignificant in the CCD columns below # 40, which were used for the analysis below.

## 2.2. Spectral analysis

Both EPIC-MOS spectra of PSR J0437–4715 were extracted from circles of a  $30''$  radius centered at the pulsar position, each containing about 82% of all detected source counts. Background was estimated from a few source-free regions. The extracted spectra were binned with at least 30 source counts per bin. The estimated total count rates of the pulsar are  $161 \pm 2$  and  $167 \pm 2$  counts  $\text{ks}^{-1}$  in the 0.3–10 keV range for the EPIC-MOS1 and MOS2

---

<sup>4</sup>European Photon Imaging Camera

<sup>5</sup><http://xmm.vilspa.esa.es>

detectors, respectively (energies below 0.3 keV were not used because of uncertainties in the EPIC-MOS calibration). The EPIC-pn spectrum was extracted from the CCD columns #28–39, what provides about 85% of all detected source counts. Background was estimated from the columns #12–23. The EPIC-pn spectrum was binned with at least 100 source counts in each bin. The total source count rate was measured to be  $674 \pm 5$  counts  $\text{ks}^{-1}$  in the 0.3–10 keV range (there is no spectral information below 0.3 keV in the EPIC-pn detector in Timing mode). All instrument response matrices and effective areas were generated with the SAS tools *rmfgen* and *arfgen* (these tools were also used in analysis of all XMM-Newton data discussed in this paper). The source count rates in the Reflection Grating Spectrometers,  $\sim 20$  counts  $\text{ks}^{-1}$ , are too low for a meaningful analysis of this data.

Applying a simple one-component model to the three combined EPIC spectra resulted in unreasonable model parameters and unacceptable fit quality. A best single (absorbed) PL fit results in a photon index of  $\Gamma \approx 3.5$  and absorbing hydrogen column density of  $n_{\text{H},20} = n_{\text{H}}/(10^{20} \text{ cm}^2) \approx 11.6$  (vs. the estimate  $n_{\text{H},20} = 0.1\text{--}0.3$  obtained from independent measurements — see Zavlin & Pavlov 1998), with the minimum value of  $\chi^2_\nu = 2.47$  (for  $\nu = 426$  degrees of freedom). Even worse fit is yielded by a one-temperature thermal model, e.g.,  $\chi^2_\nu = 7.14$  for a single blackbody (BB) spectrum, because of a large data excess at energies  $E \gtrsim 2$  keV. A two-component model, BB+PL, results in  $\chi^2_\nu = 1.67$  ( $\nu = 424$ ). With account for problems in the cross-calibration of the EPIC instruments<sup>6</sup> it can be considered as a reasonably good fit. In this model the PL component with  $\Gamma = 2.9$  provides about 70% of the observed X-ray flux ( $f_X \approx 1.1 \times 10^{-12}$  erg  $\text{s}^{-1} \text{ cm}^{-2}$  in 0.2–10 keV). However, the obtained value of  $n_{\text{H},20} = 1.4$  still significantly exceeds the independent estimates on the hydrogen column density. In addition, the inferred photon index is much larger than  $\Gamma = 1.4\text{--}2$  found in nonthermal emission from other radio (including millisecond ones) pulsars. A similar problem arises when one-temperature PC model with hydrogen atmosphere is applied. Hence, we regard this model as rather infeasible. The next option is a PC model with a nonuniform temperature distribution combined with a PL component. Applying the “core”+“rim” model for two PCs covered with a hydrogen atmosphere (Zavlin et al. 1996) and assuming standard NS mass  $M = 1.4M_\odot$  and radius  $R = 10$  km yields<sup>7</sup>  $T_{\text{pc}}^{\text{core}} = 1.4 \pm 0.2$  MK and  $T_{\text{pc}}^{\text{rim}} = 0.52 \pm 0.16$  MK (unredshifted values),  $R_{\text{pc}}^{\text{core}} = 0.35 \pm 0.18$  km and  $R_{\text{pc}}^{\text{rim}} = 2.6 \pm 0.4$  km, and  $\Gamma = 2.0 \pm 0.4$ , for  $n_{\text{H},20}$  varying between 0.1 and 0.3, with the minimal value of  $\chi^2_\nu = 1.57$  ( $\nu = 422$ ). Formally, according to an  $F$ -test, the probability that the spectral

---

<sup>6</sup>See Kargaltsev et al. (2005) for results of the spectral analysis of XMM-Newton data on the NS RX J1856.5–3754, as well as other examples at <http://xmm.vilspa.esa.es/docs/documents/CAL-TN-0018-2-4.pdf>.

<sup>7</sup>Errors in fitting parameters are given at a  $1\sigma$  level for one interesting parameter.

data on PSR J0437–4715 require a two-temperature PC model (instead of a one-temperature thermal component) is 99.99992%. This model implies equal angles  $\zeta$  (between the line-of-sight and pulsar spin axis) and  $\alpha$  (between the magnetic and spin axes) of  $45^\circ$ . Figure 3 presents a best fit with this two-component model. The estimated bolometric luminosity of two PCs is  $L_{\text{bol}} = (3.4 \pm 0.7) \times 10^{30} \text{ erg s}^{-1}$ , and the PL luminosity in 0.2–10 keV is  $L^{\text{nonth}} = (0.5 \pm 0.2) \times 10^{30} \text{ erg s}^{-1}$ . Changing the pulsar geometry (angles  $\zeta$  and  $\alpha$ ) as well as the NS mass-to-radius ratio in a plausible range  $M/R = (1.0\text{--}1.8) M_\odot/(10 \text{ km})$  responsible for the gravitational effects (redshift and bending of photon trajectories) increases the errors in the PC parameters, but insignificantly it affects the inferred thermal luminosity (see Zavlin & Pavlov 2004 for more details). Generally, the spectral results obtained from the EPIC data are in good agreement with those derived from the previous observations.

Another hypothesis is that the pulsar spectrum is of a pure nonthermal origin with the PL slope changing somewhere in the X-ray range. To verify this, a broken PL model was applied to the EPIC spectra, that yielded a best fit with  $n_{\text{H},20} = 2.3 \pm 0.5$ , and photon indices  $\Gamma_1 = 2.4 \pm 0.2$  and  $\Gamma_2 = 3.6 \pm 0.1$  below and above the break energy  $E_{\text{br}} = 1.05 \pm 0.05 \text{ keV}$  ( $\chi^2_\nu = 1.73$  for  $\nu = 424$ ). However, this model significantly overpredicts the *UV/FUV* fluxes detected from PSR J0437–4715 (Kargaltsev et al. 2004). This, together with the large value of the interstellar absorption inferred in the fit, makes the broken-PL interpretation rather implausible.

### 2.3. Timing analysis

For the timing analysis, we used 38393 counts extracted from the EPIC-pn CCD columns # 35–39 in the 0.3–6 keV range chosen to maximize the signal-to-noise ratio ( $S/N = 163$ ). Of those counts, 88% belong to the pulsar. The photon arrival times were transformed to the solar system barycenter with the *barycen* tool of the SAS package (this procedure was also applied to all other timing data discussed in this paper). As timing parameters of millisecond pulsars are known to be very stable, we invoked the binary ephemeris parameters from Zavlin et al. (2002). These parameters used in the  $Z_n^2$  test ( $n$  is number of harmonics — see Buccheri et al. 1983) yielded the most significant value  $Z_n^2 = 2170.2$  with  $n = 2$ . The maximum of  $Z_{2,\text{max}}^2 = 2199.1$  is reached at a frequency  $f$  which differs from the radio value by  $\delta f = 0.8 \mu\text{Hz}$ , corresponding to a relative accuracy,  $\delta f/f \simeq 5 \times 10^{-9}$ , consistent with that estimated for the EPIC-pn timing<sup>8</sup>.

We extracted the pulsed profiles of PSR J0437–4715 in five energy ranges, 0.3–0.5, 0.5–

---

<sup>8</sup>See <http://xmm.vilspa.esa.es/docs/documents>

0.8, 0.8–2, 0.3–2 keV, and 2–6 keV, which are given in Figure 4 together with estimated values of pulsed fraction  $f_p$ . The statistical  $\chi^2$  test described in Zavlin & Pavlov (1998) shows that the shapes of the three lower-energy light curves are actually the same (the probability that they are different is less than 90%). However, the 2–6 keV light curve seems to be more symmetric, with a peak apparently narrower than those in the lower-energy pulse profiles. One may also speculate that there is a phase shift of  $\delta\phi \sim 0.1$  between the peaks at energies below and above 2 keV. This apparent difference is supported by the same statistical test yielding a fairly high probability of 99.99997% (or a  $4.2\sigma$  significance) that the shapes of the 0.3–2 and 2–6 keV pulse profiles are different. Another feature in the extracted light curves is the change of the source intrinsic pulsed fraction with energy:  $f_p$  increases by about 10% from  $\sim 32\%$  at the lowest energies to  $\sim 42\%$  at  $E \sim 1$  keV, similar to the energy behavior of  $f_p$  first found by Becker & Trümper (1993) from the *ROSAT* data. The estimated pulsed fraction at  $E > 2$  keV is less certain because of a scantier statistics and strong background contamination at higher energies, although it may be as high as  $\sim 65\%$ . Generally, the energy dependence of the pulsar light curves can be attributed to different emission mechanisms producing the X-ray flux of PSR J0437–4715, as suggested by the thermal-plus-nonthermal model.

Figure 5 shows the pulse profiles of PSR J0437–4715 obtained from the *ROSAT* Position Sensitive Proportional Counter, *Chandra* High Resolution Camera (see Zavlin et al. 2002) and *XMM-Newton* EPIC-pn data (in 0.3–6 keV). The pulsed fractions in the latter two light curves are similar to each other and somewhat larger than that found in the *ROSAT* data. This may be explained by both the properties of the pulsar emission (increase of  $f_p$  with energy) and the greater sensitivity of the *XMM-Newton* and *Chandra* instruments to higher-energy photons. The shapes of these three light curves are clearly asymmetric, with a longer rise. This asymmetry could be caused by contribution of the nonthermal component (more than 10% at all energies) whose peak is shifted in phase with respect to the pulse of the thermal emission.

As the error in the EPIC-pn absolute timing can be as large as 0.5 ms, the phasing between the radio and X-ray peaks was not attempted (this is also one of the reasons why the zero phases in Fig. 5 are arbitrary).

## 2.4. Phase-resolved spectroscopy

In principle, the EPIC-pn data on PSR J0437–4715 allow one to perform a phase-resolved spectroscopy of the pulsar emission. To do this, we extracted the pulsar spectra in five equal intervals between the rotational phases 0 and 1, with the zero-phase as in

Figures 4 and 5, from the same CCD columns chosen for the phase-integrated spectrum (§ 2.2). The spectra were binned to collect at least 50 source counts per bin. A simplest and broadly used approach is to fit the phase-resolved spectra with the same model to determine the dependences of model parameters on rotational phase. Based on the results of § 2.2, we applied the two-temperature PC (“core”+“rim”) plus PL model with temperatures of the thermal components and photon index fixed at the best values derived for the phase-integrated spectrum. The hydrogen column density was also fixed at  $n_{\text{H},20} = 0.2$ . Figure 6 shows phase dependences of the three fitting parameters, sizes of the PCs and nonthermal flux, normalized by the corresponding values found in the phase-integrated spectral analysis. The former two represent the PC areas projected onto a plane perpendicular to the line-of-sight of a distant observer. As it could be expected, these two dependences are very similar to each other and resemble the shape of the lower-energy light curves (at  $E < 2$  keV) shown in Figure 4. On the other hand, the phase dependence of the nonthermal flux clearly differs from those of the PC areas, with a narrower peak shifted with respect to the maxima in the PC phase dependences, indicating that the shift between the peaks in the pulsed profiles of PSR J0437–4715 extracted at energies below and above 2 keV (Fig. 4) is real. Also, the modulation of the nonthermal flux is rather large, by about 60%, pointing to a high intrinsic pulsed fraction of the nonthermal component.

More detailed information could be obtained from combining the phase-resolved spectroscopy with modeling the pulsar light curves. However, such an analysis is beyond the scope of this paper.

### 3. PSR J2124–3358

X-ray emission from this solitary pulsar was first detected with *ROSAT* (Becker & Trümper 1999). These data provided a  $4\sigma$  detection of pulsations of the pulsar X-ray flux with a pulsed fraction  $f_p \sim 33\%$ . PSR J2124–3358 was also observed with *ASCA* (Sakurai et al. 2001). No significant pulsations were found in those data of a scanty statistics. The pulsar spectrum could be equally well fitted with either a single PL spectrum of photon index  $\Gamma \sim 2.8$  or a thermal BB model of a temperature<sup>9</sup>  $T_{\text{bb}}^\infty \sim 3.6$  MK emitted from an area of an apparent radius  $R_{\text{bb}}^\infty \sim 0.02$  km (for a distance  $d = 0.27$  kpc). Based on the inferred model parameters, Sakurai et al. (2001) concluded that the thermal interpretation is more plausible.

---

<sup>9</sup>The superscript “ $\infty$ ” stays for redshifted values as measured by a distant observer.



### 3.1. XMM-Newton observation

XMM-Newton observed PSR J2124–3358 on 2002 April 14–15 (orbit 430) for 68.9 and 66.8 ks effective exposure for the EPIC-MOS and EPIC-pn detectors operated with medium and thin filters, respectively, in the same observational modes as for PSR J0437–4715. Figure 7 shows a  $20' \times 20'$  combined EPIC-MOS1 and MOS2 image with the pulsar located close to the image center. With the satellite position angle of  $76.7^\circ$  in this observation, the pulsar emission detected in the EPIC-pn data was contaminated by weaker field sources (see Fig. 7 for the EPIC-pn field of view). Analysis of the 1-D distribution of EPIC-pn photons shows that the contamination is substantial only at energies  $E \gtrsim 2$  keV. Hence, the 0.3–2 keV range was used for the analysis of the pulsar radiation detected with the EPIC-pn instrument.

### 3.2. Spectral analysis

Two EPIC-MOS spectra PSR J2124–3358 were extracted from circles of a  $40''$  radius centered at the pulsar position, encircling about 88% of all detected source counts. The extracted spectra were binned with at least 25 source counts per bin. It was found that the pulsar emission is completely buried under background at energies above 3 keV. Hence, only the 0.3–3 keV range was used for the EPIC-MOS data on the pulsar (0.3 keV is the calibration “threshold” for these instruments — see § 2.2). The inferred total source count rates are  $13 \pm 2$  and  $17 \pm 2$  counts  $\text{ks}^{-1}$  for the EPIC-MOS1 and MOS2 detectors, respectively. The EPIC-pn source (plus background) spectrum was extracted from the CCD columns # 35–42 (see insert in Fig. 7). This was estimated to provide about 82% of all pulsar counts detected with EPIC-pn. Background was evaluated from the columns # 51–58. The EPIC-pn spectrum of PSR J2124–3358 in the 0.3–2 keV range was binned with at least 40 source counts in each bin. The total source count rate in this instrument is  $57 \pm 3$  counts  $\text{ks}^{-1}$ .

Estimates for the hydrogen column density in the direction to PSR J2124–3358 are rather uncertain. The pulsar dispersion measure  $DM = 4.6 \text{ pc cm}^{-3} \text{ pc}$  suggests  $n_{\text{H},20} \sim 1$ , whereas estimates<sup>10</sup> for objects close to PSR J2124–3358 indicate on larger values,  $n_{\text{H},20} \sim 3$ . The total Galactic column density in the direction to PSR J2124–3358 is  $n_{\text{HI}} \simeq 6 \times 10^{20} \text{ cm}^{-2}$ . Hence,  $n_{\text{H},20} = 1\text{--}3$  can be regarded as a plausible range. The three EPIC spectra were first fitted with a single PL model. Although this fit is formally acceptable ( $\chi^2_\nu = 1.1$  for  $\nu = 121$ ), it yielded a very large photon index  $\Gamma = 3.3 \pm 0.4$  and too high hydrogen column density  $n_{\text{H},20} = 16 \pm 5$ . These two parameters make the pure nonthermal interpretation

---

<sup>10</sup>See <http://archive.stsci.edu/euве/ism/ismform.html>

of the pulsar X-ray emission infeasible. Applying a single thermal model, either BB or one-temperature PCs with hydrogen atmosphere leaves a significant data excess at energies  $E \gtrsim 1.5$  keV, suggesting that one more component is required to fit the spectra.

First two-component model to test was one-temperature PCs with hydrogen atmosphere plus a PL spectrum. Such a model yielded a good fit with  $\chi^2_\nu = 1.1$  ( $\nu = 119$ ) and hydrogen column density  $n_{\text{H},20} = 3 \pm 2$  compatible with the independent estimates. As the pulsar emission is detected only below 3 keV, the slope of the nonthermal component is rather unconstrained,  $\Gamma = 2.1 \pm 0.7$ . Nevertheless, the (isotropic) nonthermal luminosity is well determined,  $L^{\text{nonth}} = (0.9 \pm 0.2) \times 10^{30}$  erg s $^{-1}$  in the 0.2–10 keV range (for  $d = 0.27$  kpc). The inferred PC parameters are  $T_{\text{pc}} = 1.3 \pm 0.1$  MK and  $R_{\text{pc}} = 0.32 \pm 0.04$  km (for the standard NS mass  $M = 1.4 M_\odot$  and radius  $R = 10$  km, and pulsar angles  $\zeta = \alpha = 45^\circ$ ). The corresponding bolometric luminosity of two PCs,  $L_{\text{bol}} = (1.0 \pm 0.2) \times 10^{30}$  erg s $^{-1}$ , is almost the same as the estimated PL luminosity. A best PC-plus-PL fit is shown in Figure 8. As hydrogen atmosphere spectra are much harder than the BB ones at the same effective temperature, using the BB model for the thermal component results in a higher temperature,  $T_{\text{bb}}^\infty \sim 2.4$  MK, and a much smaller radius of emitting area,  $R_{\text{bb}}^\infty \sim 0.04$  km (see, e.g., Zavlin & Pavlov 2004 for more examples).

Next, a two-temperature PC (“core”+“rim”) model was applied to the EPIC spectra of PSR J2124–3358. It yielded a fit of the same quality as the one-temperature PC plus PL fit and the following model parameters:  $T_{\text{pc}}^{\text{core}} = 2.2 \pm 0.2$  MK,  $T_{\text{pc}}^{\text{rim}} = 0.5 \pm 0.1$  MK, and  $R_{\text{pc}}^{\text{core}} = (0.11 \pm 0.03)$  km,  $R_{\text{pc}}^{\text{rim}} = (1.9 \pm 0.7)$  km (for the same assumption on the NS mass, radius and geometry as above). Interestingly, these numbers are similar to those estimated for PSR J0437–4715 (§ 2.2). The bolometric luminosity of these PCs is  $L_{\text{bol}} = (1.8 \pm 0.1) \times 10^{30}$  erg s $^{-1}$ . No other spectral component (e.g., PL) in addition to this PC model is required to fit the observed data. An upper limit on nonthermal emission of PSR J2124–3358 is  $L^{\text{nonth}} < 0.09 \times 10^{30}$  erg s $^{-1}$  (in the 0.2–10 keV range).

### 3.3. Timing analysis

To obtain a maximal signal-to-noise ratio ( $S/N = 21$ ), the EPIC-pn CCD columns #37–40 were used for extracting source (plus background) counts in the 0.3–2 keV range. Of total 8506 counts extracted, 39% was estimated to be emitted from the pulsar. Using the radio ephemeris parameters of PSR J2124–3358 from the ATNF catalog, spin frequency  $f_0 = 202.793897234988$  Hz and its derivative  $\dot{f} = -8.447 \times 10^{-16}$  s $^{-2}$  (at MJD 50288.0), in the  $Z_n^2$  test immediately revealed a signal, with the most significant component  $Z_2^2 = 97.1$ . The probability to obtain such a value by chance in one trial is  $4.1 \times 10^{-20}$ . The maximum

value  $Z_{2,\text{max}}^2 = 97.6$  is reached at a frequency which differs from  $f_0$  by  $\delta f = 0.7 \mu\text{Hz}$ , similar to the case of PSR J0437–4715 (§ 2.3).

Because of the strong background contamination and relatively narrow energy range where the pulsar data are available, only the energy-integrated (in 0.3–2 keV) light curve of PSR J2124–3358 was extracted (see Fig. 9). It reveals one broad prominent pulse per period (at phase  $\phi \approx 0.8$  in Fig. 9) and a possible weaker peak separated from the main one by  $\delta\phi \approx 0.35$  (or  $\delta\phi \approx 0.65$ , depending on which pulse is leading). Alternatively, the obtained pulse may be described as a single broad peak with an asymmetric shape, a steeper rise and a longer trail, as predicted by relativistic effects (in particular, the Doppler boost) in fast rotating pulsars (Braje et al. 2000). The estimated source intrinsic pulsed fraction,  $f_p = 56 \pm 14\%$  is fairly high, but it is still consistent with thermal PC models, depending on the NS geometry and compactness (the  $M/R$  ratio).

#### 4. PSR J1024–0719

This is a solitary pulsar with a spin period  $P \simeq 5.2$  ms, characteristic age  $\tau \simeq 4.4$  Gyr and rotational energy loss  $\dot{E} \simeq 5.3 \times 10^{33}$  erg s<sup>−1</sup> (according to the ATNF catalog). It is a relatively close object located at a distance  $d \simeq 0.39$  kpc, as derived from the pulsar dispersion measure  $DM = 6.49$  cm<sup>−3</sup> pc and the model Galactic distribution of free electrons by Cordes & Lazio (2003). From *ROSAT* data Becker & Trümper (1999) suggested an X-ray counterpart for PSR J1024–0719 (at a  $4\sigma$  significance level). Because of very poor statistics available ( $\sim 25$  counts) and properties of the instrument used in the *ROSAT* observation, neither spectral nor timing information on the pulsar X-ray counterpart could be obtained.

##### 4.1. XMM-Newton observation

PSR J1024–0719 was observed with XMM-Newton on 2003 December 2 (orbit 729) for 68.0 and 66.2 ks effective exposures for the EPIC-MOS and EPIC-pn instruments, respectively, with the same filter and observational modes as for PSR J0437–4715. Figure 10 shows a  $20' \times 20'$  combined EPIC-MOS1 and MOS2 image in the 0.3–2 keV range. PSR J1024–0719 is clearly detected at a position which differs from its radio position by only  $0''.4$ , that is well within the  $2''$ – $3''$  uncertainty of the EPIC absolute astrometry. As seen in the EPIC-MOS image, the EPIC-pn field of view contains many background sources, with a comparable (or even larger) brightnesses, which heavily contaminate the 1-D image of PSR J1024–0719 in the EPIC-pn data (see insert in Fig. 10). This makes the EPIC-pn data virtually useless

for spectral analysis of the pulsar emission because no reliable background subtraction is possible.

## 4.2. Spectral analysis

Only EPIC-MOS data were used to evaluate spectral properties of PSR J1024–0719. The pulsar counts were extracted from circles of a  $20''$  radius, which contain about 70% of all photons detected from PSR J1024–0719. Background was estimated from a few source-free regions. The extracted spectra were binned with at least 20 source counts per bin in the 0.3–2 keV range and 9–11 source counts in the bins at 2–3 keV. The total source count rates are  $2.3 \pm 0.3$  and  $2.7 \pm 0.3$  counts  $\text{ks}^{-1}$  for the EPIC-MOS1 and MOS2 detectors, respectively.

The pulsar dispersion measure gives a hydrogen column density  $n_{\text{H},20} \sim 2$  toward PSR J1024–0719. Independent estimates of interstellar absorption for objects close to the pulsar suggest  $n_{\text{H},20} \sim 6$ , whereas the total Galactic column density is  $n_{\text{HI}} \simeq 5 \times 10^{20} \text{ cm}^{-2}$ . A single PL fit to the pulsar spectra produced a best result with  $\Gamma = 3.7 \pm 0.8$  and  $n_{\text{H},20} = 23 \pm 5$  ( $\chi^2_\nu = 1.4$  for  $\nu = 11$ ). Similar to the case of PSR J2124–3358, these inferred parameters make the pure nonthermal interpretation hardly plausible. A single BB model fits the spectra equally well ( $\chi^2_\nu = 1.1$ ). The obtained parameters are  $n_{\text{H},20} = 2 \pm 2$  (compatible with the independent estimates),  $T_{\text{bb}}^\infty = 2.9 \pm 0.3$  MK and  $R_{\text{bb}}^\infty = 0.03 \pm 0.01$  km (for  $d = 0.39$  kpc). One-temperature PC model with nonmagnetic hydrogen atmosphere (and the same assumption on the NS parameters as in §§ 2.2 and 3.2) yielded  $T_{\text{pc}} = 1.8 \pm 0.4$  MK and  $R_{\text{pc}} = 0.1 \pm 0.1$  km ( $\chi^2_\nu = 1.0$ ), and the same  $n_{\text{H},20}$  range as in the BB fit. A best PC model is shown in Figure 11. The estimated bolometric luminosity of two PCs is  $L_{\text{bol}} = (0.4 \pm 0.2) \times 10^{30} \text{ erg s}^{-1}$ . Adding a PL component of  $\Gamma = 2$  to the best PC model fit put virtually the same upper limit on the nonthermal flux in the 0.2–10 keV range,  $L^{\text{nonth}} < 0.08 \times 10^{30} \text{ erg s}^{-1}$ , as found for PSR J2124–3358 in the two-temperature PC interpretation (§ 3.2). On the other hand, one can assume that the above-mentioned PC model is in fact the PC “core” and estimate temperature and size of the PC “rim” adding second thermal component. We found that to obtain a “rim” radius compatible with the estimates found for PSRs J0437–4715 and J2124–3358, a larger hydrogen density or smaller “core” radius is required. For example, if the PC “rim” temperature and radius are  $T_{\text{pc}}^{\text{rim}} = 0.4$  MK and  $R_{\text{pc}}^{\text{rim}} = 1.1$  km, then the other three parameters can be  $n_{\text{H},20} = 3$ ,  $T_{\text{pc}}^{\text{core}} = 2.1$  MK and  $R_{\text{pc}}^{\text{core}} = 0.07$  km, or  $n_{\text{H},20} = 6$ ,  $T_{\text{pc}}^{\text{core}} = 1.7$  MK and  $R_{\text{pc}}^{\text{core}} = 0.15$  km. We note that although there exist many such combinations of model parameters, the main contribution to the thermal luminosity, about 75%, comes from the softer (“core”) component as determined in the one-temperature PC fit.

### 4.3. Timing analysis

The pulsar radio ephemeris parameters from the ATNF catalog,  $f_0 = 193.71568669103$  Hz and  $\dot{f} = -6.953 \times 10^{-16} \text{ s}^{-2}$  (at MJD 51018.0), were used for searching pulsations in the X-ray flux detected from PSR J1024–0719 with the EPIC-pn instrument. An optimal column interval in the 1-D distribution of EPIC-pn counts (Fig. 10) was determined with the aid of the  $Z_1^2$  test (other harmonics with  $n > 1$  were found to be less significant). It gave  $Z_1^2 = 36.1$  for 854 source-plus-background counts extracted from the CCD columns # 38–39 in the 0.3–2 keV range. Varying spin frequency in vicinity of  $f_0$  resulted in a maximal value  $Z_{1,\text{max}}^2 = 39.1$  at a frequency differing by  $\delta f = 2.3 \text{ } \mu\text{Hz}$  from  $f_0$ . The relative deviation,  $\delta f/f = 1.2 \times 10^{-8}$ , is still consistent with the EPIC-pn timing accuracy. This value  $Z_{1,\text{max}}^2$  corresponds to a signal detection at a  $6\sigma$  significance level (probability to obtain this value by chance in one trial is  $3 \times 10^{-9}$ ).

Figure 12 presents the light curve of PSR J1024–0719 extracted in the 0.3–2 keV range. The pulse profile reveals a single broad peak per period, in agreement with the result of the  $Z_n^2$  test. To determine the intrinsic source pulsed fraction, we first estimated how many photons of those 854 extracted belong to the pulsar. To do this, 1-D count distribution were constructed from EPIC-MOS photons detected in the EPIC-pn field of view divided in two parts, with and without the pulsar emission (see caption to Fig. 10), similar to what was done for PSR J0437–4715. It gave an estimate of 34% on the fraction of pulsar photons in the total number of EPIC-MOS counts of  $E = 0.3\text{--}2$  keV extracted in the CCD columns # 38–39. Assuming that the same fraction stays for the EPIC-pn photons<sup>11</sup> gives the intrinsic pulsed fraction of about 52%, with a rather large error.

## 5. PSR J0034–0534

It is the third fastest pulsar known, with a spin period  $P \simeq 1.9$  ms. This pulsar is in a circular binary system with a low-mass companion and 1.6 d orbital period. The standard estimates give its characteristic age  $\tau \simeq 6$  Gyr, rotational energy loss  $\dot{E} \simeq 3.0 \times 10^{34} \text{ erg s}^{-1}$ , and a distance to the pulsar  $d \simeq 0.54$  kpc. In earlier years PSR J0034–0534 was observed in X-rays only with *BeppoSAX* (in July 1999 for about 100 ks), but the pulsar was not detected.

---

<sup>11</sup>This assumption may not be very accurate because of, e.g., different internal background in the EPIC-MOS and EPIC-pn instruments.

*XMM-Newton* was pointed at PSR J0034–0534 on 2002 June 16 (orbit 463) for 35.0 and 32.1 ks effective exposures with the EPIC-MOS and EPIC-pn detectors, respectively, with medium filters and the same observational modes as in the observations of the other three pulsar described §§ 2–4. A  $20' \times 20'$  combined EPIC-MOS1 and MOS2 image is shown in Figure 13. In this image an X-ray source is evident at a position which differs by only  $0''.2$  from the radio position of PSR J2124–3358. Unfortunately, in the EPIC-pn observation with the satellite position angle of  $65.5^\circ$  this X-ray source was completely buried under emission from the much brighter (by a factor of 10) object indicated with the label “S” in the image. Therefore, neither spectral nor temporal information on this source could be obtained from the EPIC-pn data (timing analysis of EPIC-pn counts extracted at the source position revealed no pulsations). The count rates of the source at the pulsar position are  $0.9 \pm 0.5$  and  $1.3 \pm 0.5$  counts  $\text{ks}^{-1}$  in the EPIC-MOS1 and MOS2 detectors, respectively. Despite the low ( $< 3\sigma$ ) formal significance of the X-ray detection, the proximity of this source to the radio position of PSR J0034–0534 makes it a likely X-ray counterpart of the pulsar. About 70 counts detected from this source with the two EPIC-MOS detectors at  $E \lesssim 3$  keV can be equally well fitted with a single PL spectrum of  $\Gamma \sim 2.5$  or a single BB model of  $T_{\text{bb}}^\infty \sim 2.2$  MK and  $R_{\text{bb}}^\infty \sim 0.05$  km (for  $d = 0.54$  kpc). Both these models yields an X-ray luminosity  $L_X \sim 0.4 \times 10^{30}$  erg  $\text{s}^{-1}$ .

## 6. Discussion and conclusion

The new *XMM-Newton* observations have enabled us to perform the spectral and timing analyses of the X-ray data collected from three pulsars, J0437–4715, J2124–3358, and J1024–0719. In addition, a possible X-ray counterpart of PSR J0034–0534 has been found, with an estimate on its X-ray flux. For the first three objects the *XMM-Newton* data have revealed strong evidences of presence of thermal components in their X-ray emission. These components are interpreted as radiation emitted from heated PCs around magnetic poles on the NS surface.

In the case of PSR J0437–4715, the new data confirmed the main result obtained from the previous observations that the pulsar spectrum is best fitted with a two-temperature PCs model with nonmagnetic hydrogen atmosphere plus a nonthermal (PL) component which contributes mainly at energies  $E \gtrsim 3$  keV. In this interpretation, the PC temperature changes from about  $\sim 1.5$  MK in the PC “core” of a  $\sim 0.4$  km radius down to  $\sim 0.5$  MK in the PC “rim” of a  $\sim 2.5$  km radius. The *XMM-Newton* data allowed us to investigate the energy-resolved pulse profiles in a broad range of  $E = 0.3$ –6 keV, as well as perform phase-resolved spectroscopy. This analysis showed that the pulse shape is different at lower and

higher energies (below and above  $\sim 2$  keV), with pulsed fraction  $f_p$  increasing by about 10% in the 0.3–2 keV range where the thermal emission dominates. This increase of  $f_p$  can be explained by the anisotropic properties of radiation emitted from a NS hydrogen atmosphere (see Zavlin et al. 1996, and Zavlin & Pavlov 1998 for more details). The pulsed fraction in the light curve extracted at energies above 2 keV is rather large,  $f_p \approx 60\%$ . In addition, the peak in the pulse profile obtained at higher energies is narrower than the pulse in the low-energy light curve and shifted by about 0.1 in phase. These properties provide strong evidence that two different emission mechanisms generate the X-ray emission of PSR J0437–4715.

The *XMM-Newton* spectral data on PSR J2124–3358 can be most plausibly interpreted as either a combination of a one-temperature PC model plus a nonthermal PL spectrum or a pure thermal radiation from PCs with a nonuniform temperature decreasing from  $\sim 2$  MK to  $\sim 0.5$  MK in the “core” and “rim” areas of the PCs, similar to that derived for PSR J0437–4715. Comparing the PC radii inferred in these two approaches — about 0.3 km with the PC-plus-PL combination and 1–2 km in the two-temperature PC model — with the canonical estimate of pulsar models,  $R_{pc}^* = R(2\pi R/cP)^{1/2} \simeq 2.1$  km for PSR J2124–3358 (assuming the NS radius  $R = 10$  km), suggests that the pure thermal interpretation is preferable. In any case, the thermal luminosities derived in these model fits differ insignificantly, by only a factor of  $\sim 2$ . In addition, the new data allowed us to firmly detect pulsations of the X-ray flux of PSR J2124–3358 at the radio pulsar period, although the shape of the obtained pulse profile cannot be interpreted unambiguously. It may be described as a profile with two peaks of different heights separated by about 0.35 (or 0.65) in phase. If so, it would suggest that two different components are detected in the pulsar emission. On the other hand, it could be a broad single peak produced by thermal PC emission with a shape distorted by the relativistic effects in fast rotating NSs.

For PSR J2124–3358, the *XMM-Newton* observation provided the first firm detection of the pulsar X-ray emission. Although the obtained statistics is much poorer than that delivered in the observations of PSR J2124–3358 and, especially PSR J0437–4715, it has shown that the pulsar’s spectrum is best described as a pure thermal radiation emitted from PCs with either uniform or nonuniform (“core”+“rim”) temperature. The derived total thermal luminosity is almost independent on assumption about the PC temperature distribution. In addition to the spectral analysis, the new data revealed pulsations of the pulsar X-ray flux at a highly significant level. Most likely, the pulsar light curves shows a single broad pulse per rotational period, although much better statistics is required to draw more definitive conclusions on the pulse shape.

Regarding the *XMM-Newton* observation of PSR J0034–0534, only a possible X-ray counterpart of the pulsar could be suggested based on the very close proximity of this source

to the pulsar position. A longer observation, with a proper satellite position angle, is needed to perform a meaningful investigation of X-ray radiation of this pulsar.

With a sample of millisecond pulsars showing thermal PC emission available (see Table 2), it is natural to compare observational properties of the PC radiation, first of all, the luminosities, with those predicted by pulsar models. A most recent and detailed analysis of PC heating is presented in Harding & Muslimov (2001, 2002) who modified the space charge limited flow model by Arons (1981) to account for the relativistic effects and electric field screening above the NS surface. In these models the PC heating is produced by inverse Compton scattering (ICS) of thermal X-rays from the NS surface by primary electrons accelerated in the pulsar magnetosphere, as well as by positrons generated through curvature radiation (CR) and returning to the NS surface from the upper pair formation front. These authors showed that the PC heating from the CR pair fronts dominates for most pulsars except those with very short spin periods and low magnetic fields (see Fig. 1 in Harding & Muslimov 2002) because the latter objects cannot produce CR pairs. Therefore, the ICS is the only mechanism to heat PCs of millisecond pulsars. Harding & Muslimov (2002) calculated the “PC efficiency” of one PC,  $\eta^{\text{pc}} = L_{\text{bol}}^{\text{pc}}/\dot{E}$ , for typical parameters of millisecond pulsars (age  $\tau = 0.1\text{--}10$  Gyr, spin period  $P = 2\text{--}5$  ms). This model predicts  $\eta^{\text{pc}}$  ranging between about  $5 \times 10^{-7}$  and  $5 \times 10^{-5}$  for PCs with temperatures  $T_{\text{pc}} = 1\text{--}3$  MK (see Fig. 8 in Harding & Muslimov 2002). Comparing these estimates with those derived from the observations (Table 2) shows that the maximum predicted value of  $\eta_{\text{max}}^{\text{pc}}$  is lower by a factor of 10 than the results obtained for PSRs J0437–4715 and J0030+0451, and a factor of 6 for PSR J2124–3358. This difference is larger for PSR J1012+5307, but we note that the  $\eta^{\text{pc}}$  value given in Table 2 for this pulsar was obtained under assumption that all X-ray flux detected from PSR J1012+5307 is of a thermal origin. For PSR J1024–0719, the value of  $\eta_{\text{max}}^{\text{pc}}$  well agrees with the observational result. On the other hand, the predicted PC luminosities,  $L_{\text{bol}}^{\text{pc}} \sim 10^{29}\text{--}10^{30}$  erg s $^{-1}$  for  $T_{\text{pc}} = 1$  MK and up to  $10^{31}$  erg s $^{-1}$  for  $T_{\text{pc}} = 3$  MK (see Fig. 9 in Harding & Muslimov 2002), are in much better agreement with those estimated for the objects listed in Table 2. To conclude, the PC heating from ICS pairs is a promising model for interpreting properties of thermal PC emission observed from millisecond pulsars.

Finally, as mentioned in § 1, there is no clear understanding yet at which conditions the thermal PC component is expected to dominate over the nonthermal one in X-ray radiation of millisecond pulsars. Saito et al. (1997) first suggested that high luminosity of the nonthermal emission may be associated with large values of the magnetic field at the pulsar light cylinder,  $B_{\text{lc}} = B_{\text{surf}}[R/R_{\text{lc}}]^3$  ( $R_{\text{lc}} = cP/2\pi$ ). Indeed, the four pulsars emitting pure nonthermal emission, PSRs B1937+21, B1957+20, B1821–24, and J0218+4232 (see § 1 and Table 1), possess magnetic fields,  $B_{\text{lc}} \sim (0.3\text{--}1) \times 10^6$  G, close to that of the Crab pulsar ( $\simeq 1 \times 10^6$  G) and exceeding those in the millisecond pulsars with thermal emission,  $B_{\text{lc}} \sim (2\text{--}3) \times 10^4$



G, at least by an order of magnitude. This provides a strong indication that the nonthermal emission of millisecond pulsars is generated in emission zone(s) close to the light cylinder (as predicted by the outer-gap pulsar models — see, e.g., Cheng et al. 1986) and  $B_{lc}$  is one of the main parameters to govern the magnetospheric activity.

The author thanks George Pavlov for helpful and stimulating discussions. This work is supported by a National Research Council Research Associateship Award at NASA MSFC.

## REFERENCES

- Arons, J. 1981, *ApJ*, 248, 1099
- Becker, W., & Trümper 1993, *Nature*, 365, 528
- Becker, W., & Trümper 1999, *A&A*, 341, 803
- Becker, W., & Aschenbach, B. 2002, in *Neutron Stars, Pulsars and Supernova Remnants*, Proc. of the 270-th Heraeus Seminar, ed. W. Becker, H. Lesch & J. Trümper (MPE Report 278), 64
- Becker, W., et al. 2003, *ApJ*, 594, 798
- Buccheri, R., et al. 1983, *A&A*, 128, 245
- Braje, T. M., Romani, R. W., & Rauch, K. P. 2000, *ApJ*, 531, 447
- Cheng, K. S., Ho, C. Ruderman, M. 1986, *ApJ*, 300, 500
- Cordes, J. M., & Lazio, T. J. W. 2003, preprint (astro-ph/0301598).
- Grindlay, J. E., Camilo, F., Heinke, C. O., Edmonds, P. D., Cohn, H., & Lugger, P. 2002, *ApJ*, 581, 470
- Harding, A. K., & Muslimov, A. G. 2001, *ApJ*, 556, 987
- Harding, A. K., & Muslimov, A. G. 2002, *ApJ*, 568, 862
- Kargaltsev, O., Pavlov, G. G., & Romani, R. W. 2004, *ApJ*, 602, 327
- Kargaltsev, O. Y., Pavlov, G. G., Zavlin, V. E., & Romani, R. W. 2005, *ApJ*, 625, 307
- Kaspi, V. M., Roberts, M. S. E., & Harding, A. K. 2006, in *Compact Stellar X-ray Sources*, ed. W. H. G. Lewin & M. van der Klis, in press (astro-ph/0402135)

- Kuiper, L., & Hermsen, W. 2004, in X-ray and Gamma-ray Astrophysics of Galactic Sources, Proc. of the 4-th AGILE Science Workshop, ed. M. Tavani, A. Pellizzoni & S. Vercellone, p. 47 (astro-ph/0312204)
- Nicastro, L., Cusumano, G., Löhmer, O., Kramer, M., Kuiper, L., Hermsen, W., Mineo, T., & Becker, W. 2004, *A&A*, 413, 1065
- Pavlov, G. G., Zavlin, V. E., & Sanwal, D. 2002, in Neutron Stars, Pulsars and Supernova Remnants, Proc. of the 270-th Heraeus Seminar, ed. W. Becker, H. Lesch & J. Trümper (MPE Report 278), 283
- Saito, Y., Kawai, N., Kamae, T., Shibata, S., Dotani, T., & Kulkarni, S. N. 1997, *ApJL*, 477, 37
- Sakurai, I., Kawai, N., Torii, K., Negoro, H., Nagase, F., Shibata, S., & Becker, W. 2001, *PASJ*, 53, 535
- Stappers, B. W., Gaensler, B. M., Kaspi, V. M., van der Klis, M., & Lewin, W. H. G. 2003, *Science*, 299, 1372
- Takahashi, M., et al. 2001, *ApJ*, 554, 316
- Taylor, J. H., Manchester, R. N., & Lyne, A. G. 1993, *ApJS*, 88, 529
- Webb, N. A., Olive, J.-F., & Barret, D. 2004a, *A&A*, 417, 181
- Webb, N. A., Olive, J.-F., Barret, D., Kramer, M., Cognard, I., & Löhmer, O. 2004b, *A&A*, 419, 269
- Zavlin, V. E., & Pavlov, G. G. 1998, 329, 583
- Zavlin, V. E., & Pavlov, G. G. 2004, *ApJ*, 616, 452
- Zavlin, V. E., & Pavlov, G. G., & Shibano, Yu. A. 1996, *A&A*, 315, 141
- Zavlin, V. E., Pavlov, G. G., Sanwal, D., Manchester, R. N., Trümper, J., Halpern, J. P., & Becker, W. 2002, *ApJ*, 569, 894

Table 1. Properties of nine millisecond pulsars<sup>a</sup>

PSR	$P$ (ms)	$d$ (kpc)	$\tau$ (Gyr)	$\log \dot{E}$ (erg s <sup>-1</sup> )	$\log L_X$ (erg s <sup>-1</sup> )	Refs.
B1937+21	1.56	3.57	0.24	36.04	33.15	1,2
B1957+20	1.61	2.49	2.24	35.20	31.81	3
J0218+4232	2.32	2.67	0.48	35.38	32.54	4
B1821–24	3.05	3.09	0.03	36.34	32.71	5
J0751+1807	3.48	1.15	7.08	33.86	30.84	6
J0030+0451	4.87	0.32	7.71	33.53	30.40	7
J2124–3358	4.93	0.27	3.80	33.83	30.23	8
J1012+5307	5.26	0.41	4.86	33.67	30.38	6
J0437–4715	5.76	0.14	4.89	33.58	30.46	9

<sup>a</sup> Based on results obtained in previous works (see references below).

Note. — Second through fourth columns give standard pulsar parameters: spin periods  $P$ , distances  $d$ , characteristic ages  $\tau$ , and rotation energy losses  $\dot{E}$ . All distances are estimated from the pulsar dispersion measures and the model of Galactic distribution of free electrons (Cordes & Lazio 2003), except for PSR J0437–4715 with the distance determined from the pulsar’s parallax (van Straten et al. 2001). The fifth column provides pulsars’ X-ray luminosities in the 0.2–10 keV range as derived in the corresponding references (sixth column): 1 – Takahashi et al. (2001), 2 – Nicastro et al. (2004), 3 – Stappers et al. (2003), 4 – Webb et al. (2004a), 5 – Becker et al. (2004), 6 – Webb et al. (2004b), 7 – Becker & Aschenbach (2002), 8 – Sakurai et al. (2001) 9 – Zavlin et al. (2002)

Table 2. Thermal luminosities of millisecond pulsars

PSR	$\log \dot{E}$ (erg s <sup>-1</sup> )	$\log L_{\text{bol}}^{\text{pc}}$ (erg s <sup>-1</sup> )	$\log \eta^{\text{pc}}$
J0437–4715	33.58	30.23	-3.35
J2124–3358	33.83	29.96	-3.87
J1024–0719	33.72	29.27	-4.45
J1012+5307 <sup>a</sup>	33.67	30.52	-3.15
J0030+0451	33.53	30.18	-3.35

Note. — The thermal (bolometric) luminosities of one PC are determined as  $L_{\text{bol}}^{\text{pc}} = L_{\text{bol}}/2$ , with  $L_{\text{bol}}$  estimates obtained in this work for the first three pulsars. For PSRs J0030+0451 and J1012+5307 the PC luminosities are calculated as  $L_{\text{bol}}^{\text{pc}} = g_r^{-2} L_{\text{bol}}^{\infty}/2$ , where  $L_{\text{bol}}^{\infty}$  are luminosities derived from BB spectral fits by Becker & Aschenbach (2002) and Webb et al. (2004b), respectively, and  $g_r = [1 - 2GM/c^2 R]^{-1/2}$  ( $= 0.77$  for  $M = 1.4 M_{\odot}$  and  $R = 10$  km). The “PC efficiency” is defined as  $\eta^{\text{pc}} = L_{\text{bol}}^{\text{pc}}/\dot{E}$ .

<sup>a</sup> Assuming that all flux detected for this pulsar is of a thermal origin.

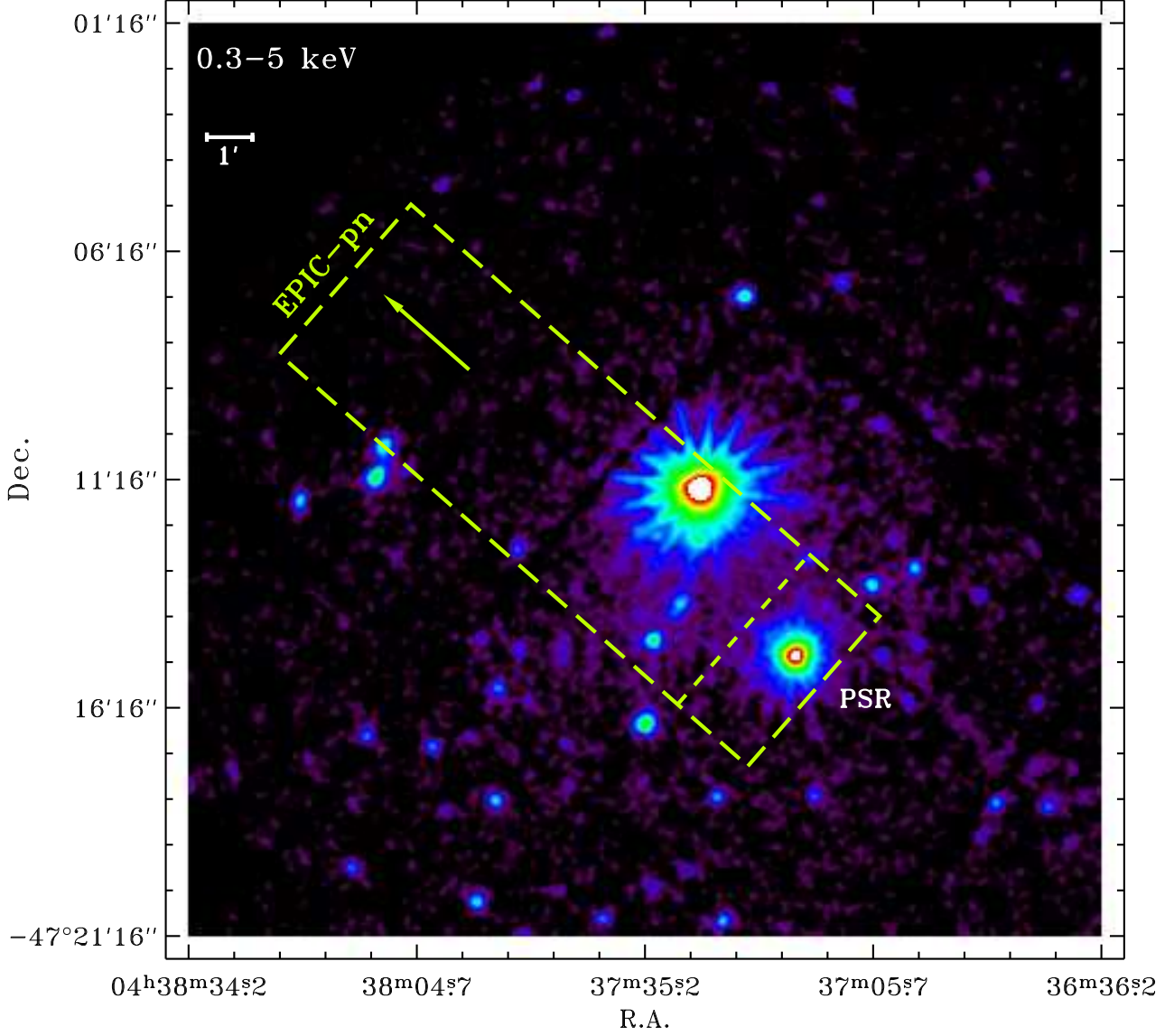


Fig. 1.— Combined EPIC-MOS1 and MOS2 image in the 0.3–5 keV range, with PSR J0437–4715 marked with the label “PSR”. Long-dashed rectangle depicts the field of view of the EPIC-pn CCD used in the *XMM-Newton* observation of the pulsar. Arrow shows the direction of the CCD read-out perpendicular to which EPIC-pn counts were collapsed in a 1-D distribution (see Fig. 2). Short-dashed line separates the areas within the EPIC-pn field of view with negligible contributions from the pulsar and AGN emission (above and below the line, respectively).

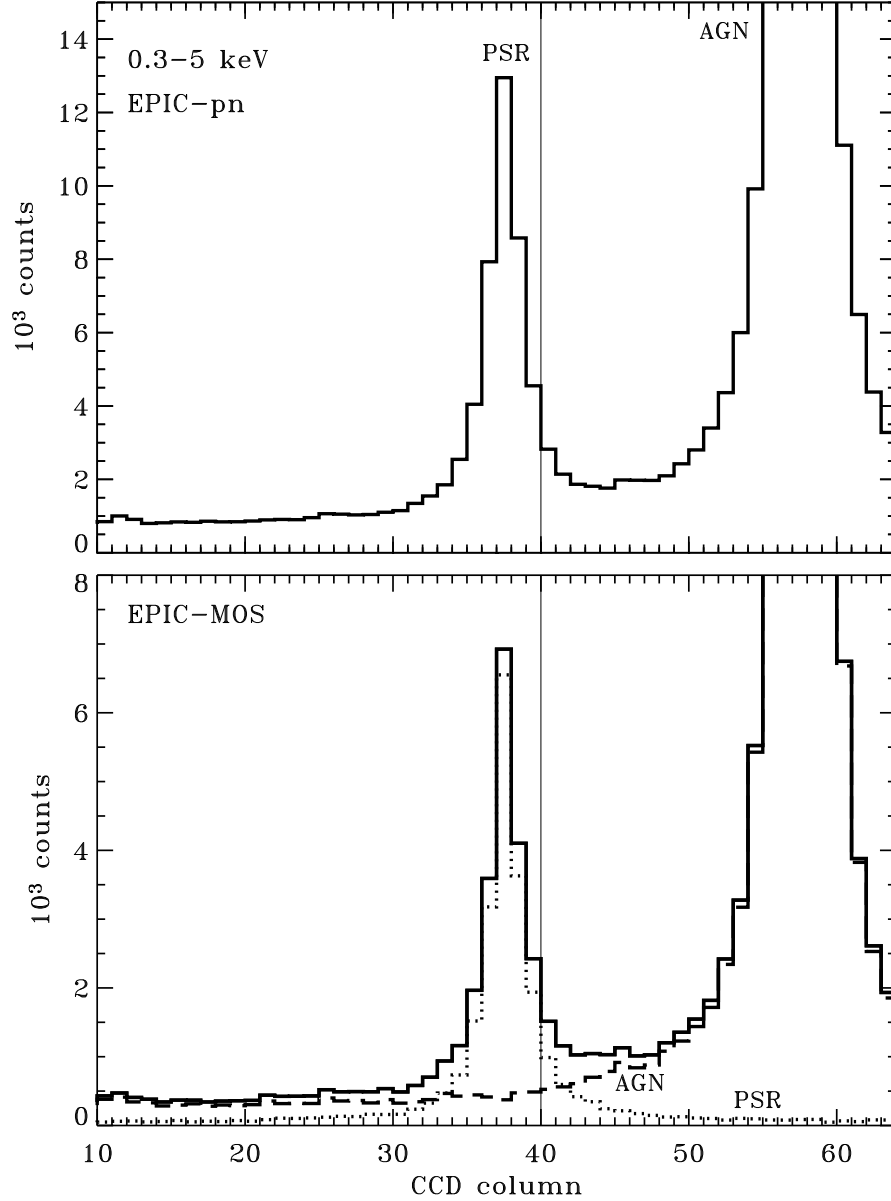


Fig. 2.— *Upper panel:* 1-D distribution of EPIC-pn counts in the 0.3-5 keV range. Peaks labeled with “PSR” and “AGN” are the images of PSR J0437–4715 and the neighboring AGN (see Fig. 1 and text). One CCD column has a width of  $4''.2$ . *Lower panel:* 1-D image (solid line) constructed from the combined EPIC-MOS1 and MOS2 data confined within the EPIC-pn filed of view drawn in Fig. 1. Dotted (labeled with “PSR”) and dashed (labeled with “AGN”) histograms show 1-D EPIC-MOS images computed for the lower and upper areas of the EPIC-pn field of view (below and above the short-dashed line in Fig. 1, respectively). Thin vertical lines in the both panels indicate the CCD column below which contamination of the pulsar emission by that from the AGN is negligible.

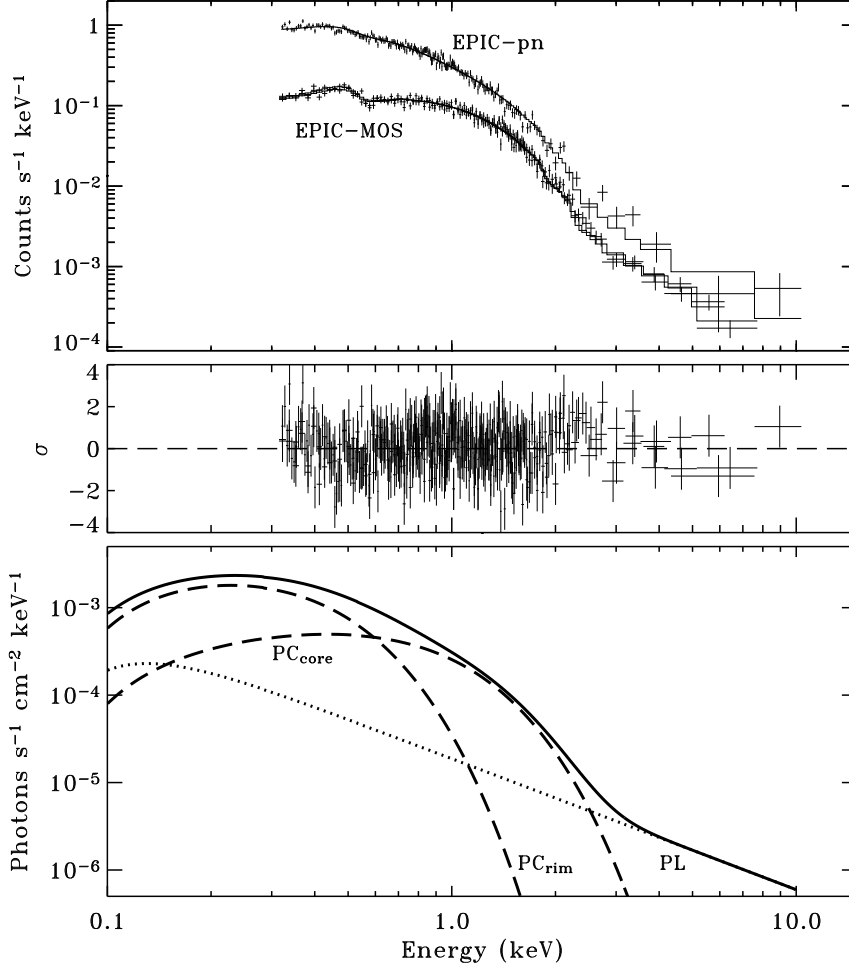


Fig. 3.— EPIC-pn and two EPIC-MOS phase-integrated spectra of PSR J0437–4715 fitted with a best two-temperature polar cap (PC) model (“core”+“rim”) plus a power-low (PL) component, residuals of the fit, and model fluxes (*upper*, *middle*, and *lower panels*, respectively).

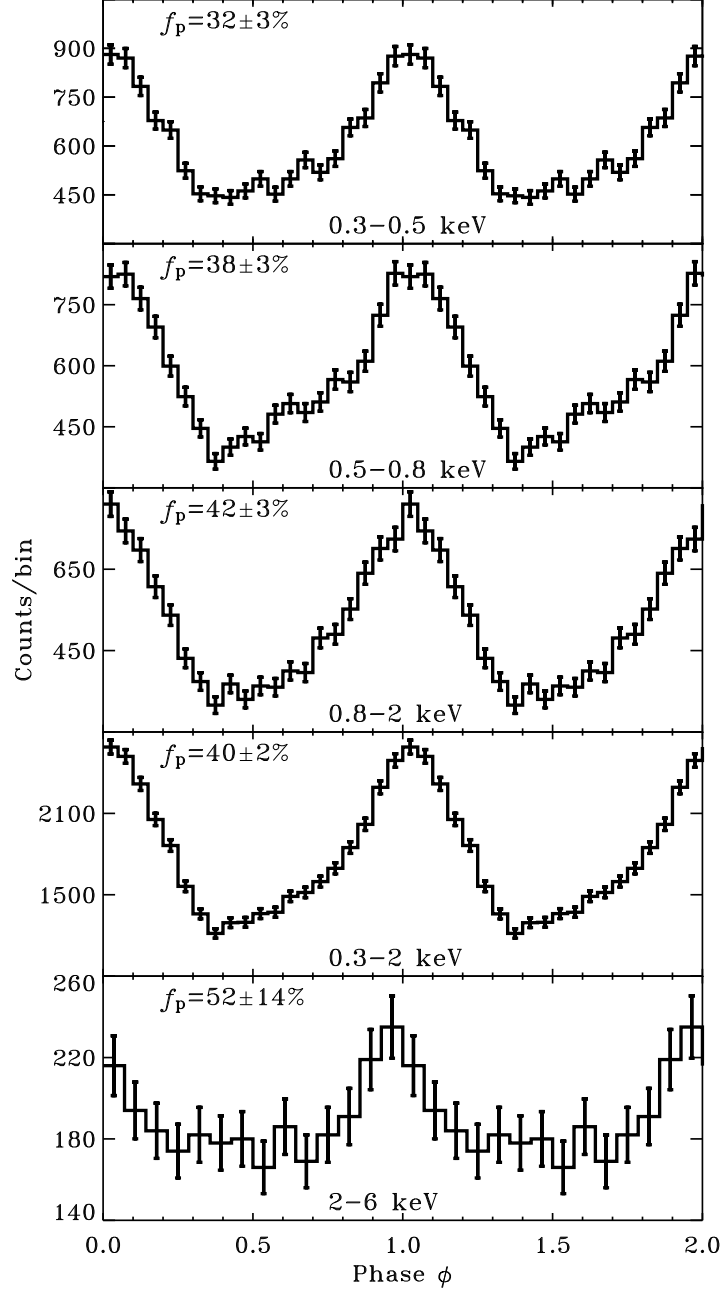


Fig. 4.— Energy-resolved pulsed profiles of PSR J0437–4715 extracted from the EPIC-pn data, with estimated values of the intrinsic source pulsed fraction  $f_p$ .



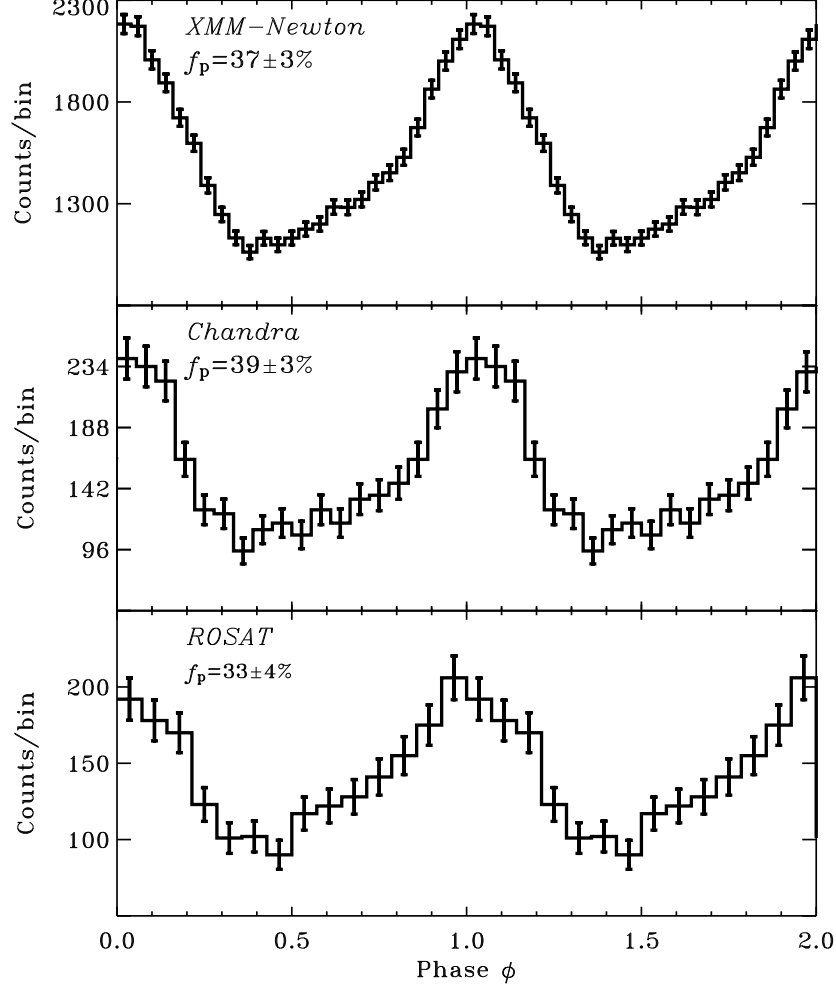


Fig. 5.— Pulsed profiles of PSR J0437–4715 obtained from the *XMM-Newton* (0.3–6 keV), *Chandra* (0.1–10 keV) and *ROSAT* (0.1–2.4 keV) data, with estimated values of the intrinsic source pulsed fraction  $f_p$ . Zero phases are arbitrary.

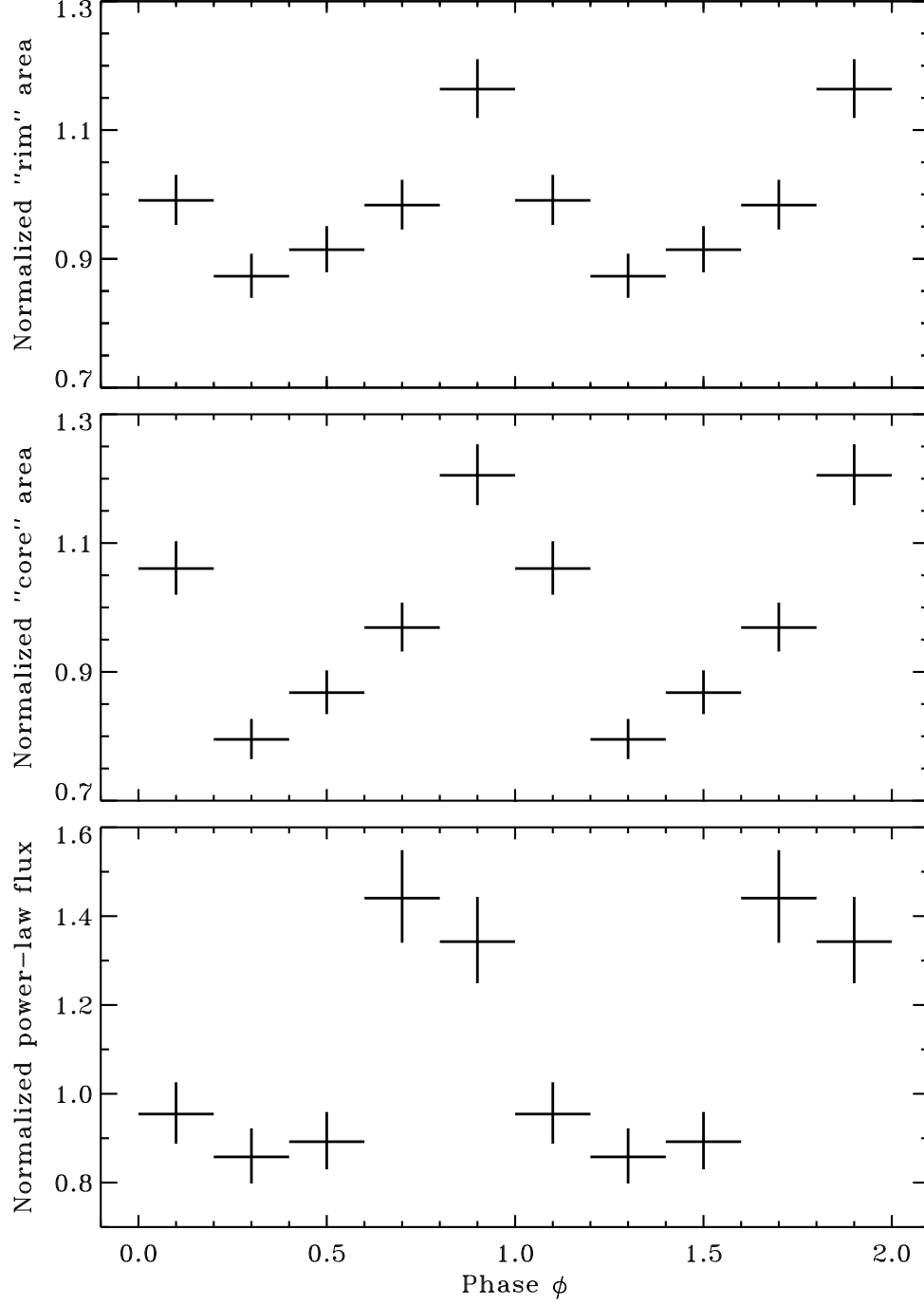


Fig. 6.— Phase dependences of the polar cap (PC) areas and nonthermal (PL) flux in the two-temperature PC (“core”+“rim”) plus PL model.

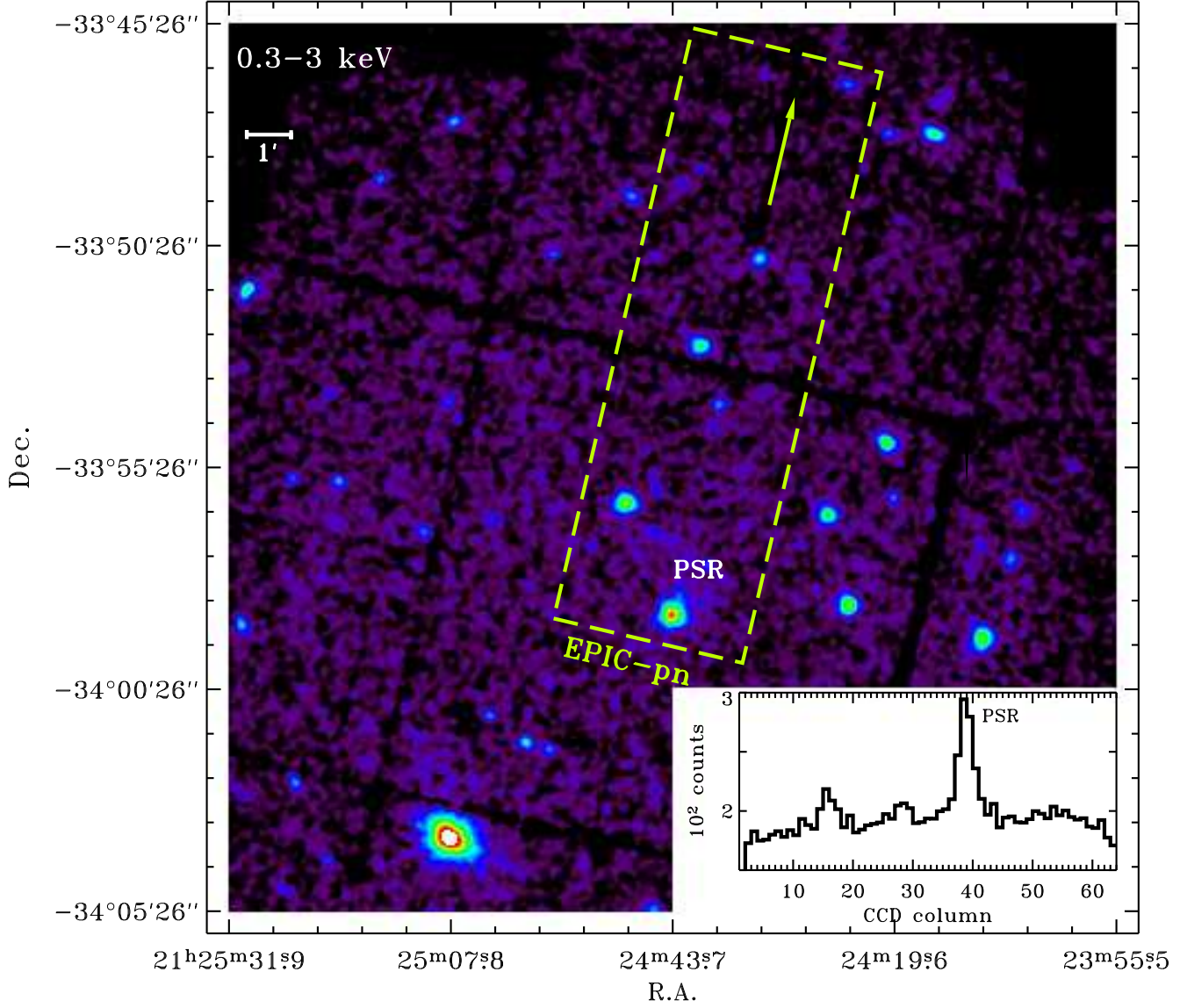


Fig. 7.— Combined EPIC-MOS1 and MOS2 image in the 0.3–3 keV range, with PSR J2124–3358 marked with the label “PSR” (see caption to Fig. 1 for other details). One-dimensional distribution of EPIC-pn counts is shown in the insert.

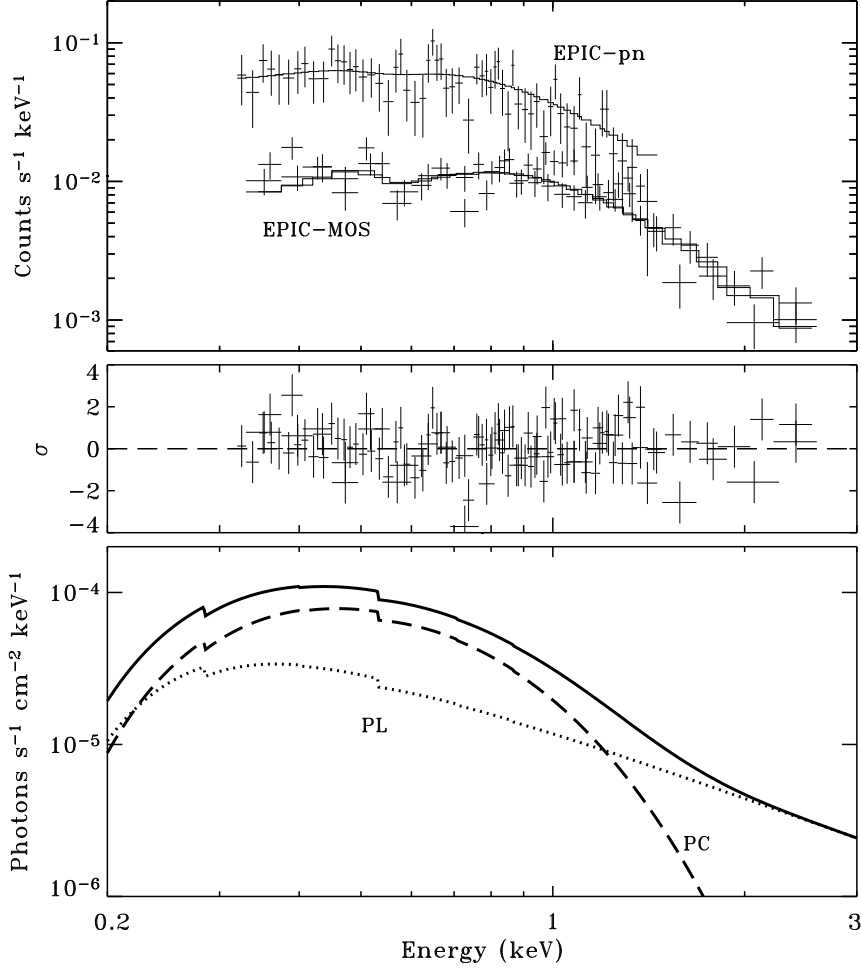


Fig. 8.— EPIC-pn and two EPIC-MOS phase-integrated spectra of PSR J2124–3358 fitted with a two-component (polar cap [PC] plus a power-low [PL]) model, residuals of the fit, and model fluxes (*upper, middle, and lower panels, respectively*).

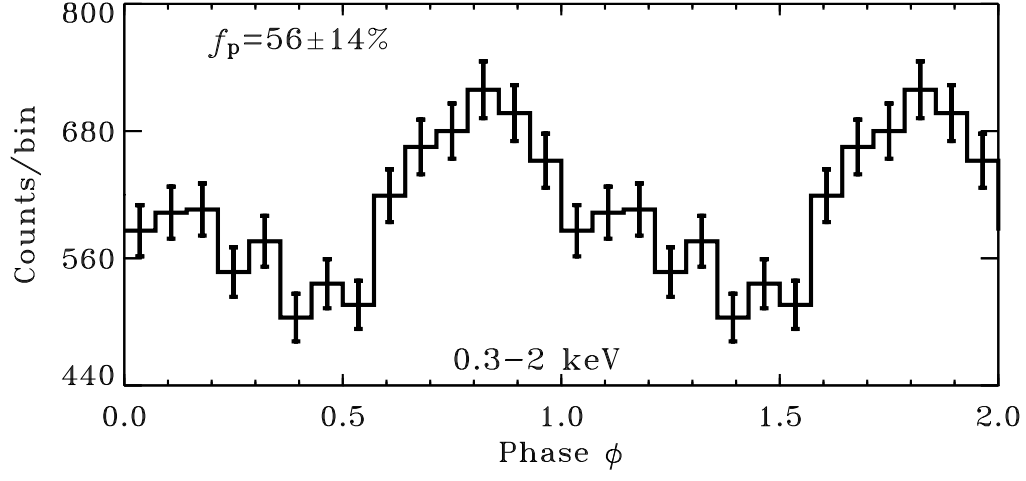


Fig. 9.— Pulse profile of PSR J2124–3358 extracted from the EPIC-pn data in the 0.3–2 keV range, with estimated value of the intrinsic source pulsed fraction  $f_p$ .

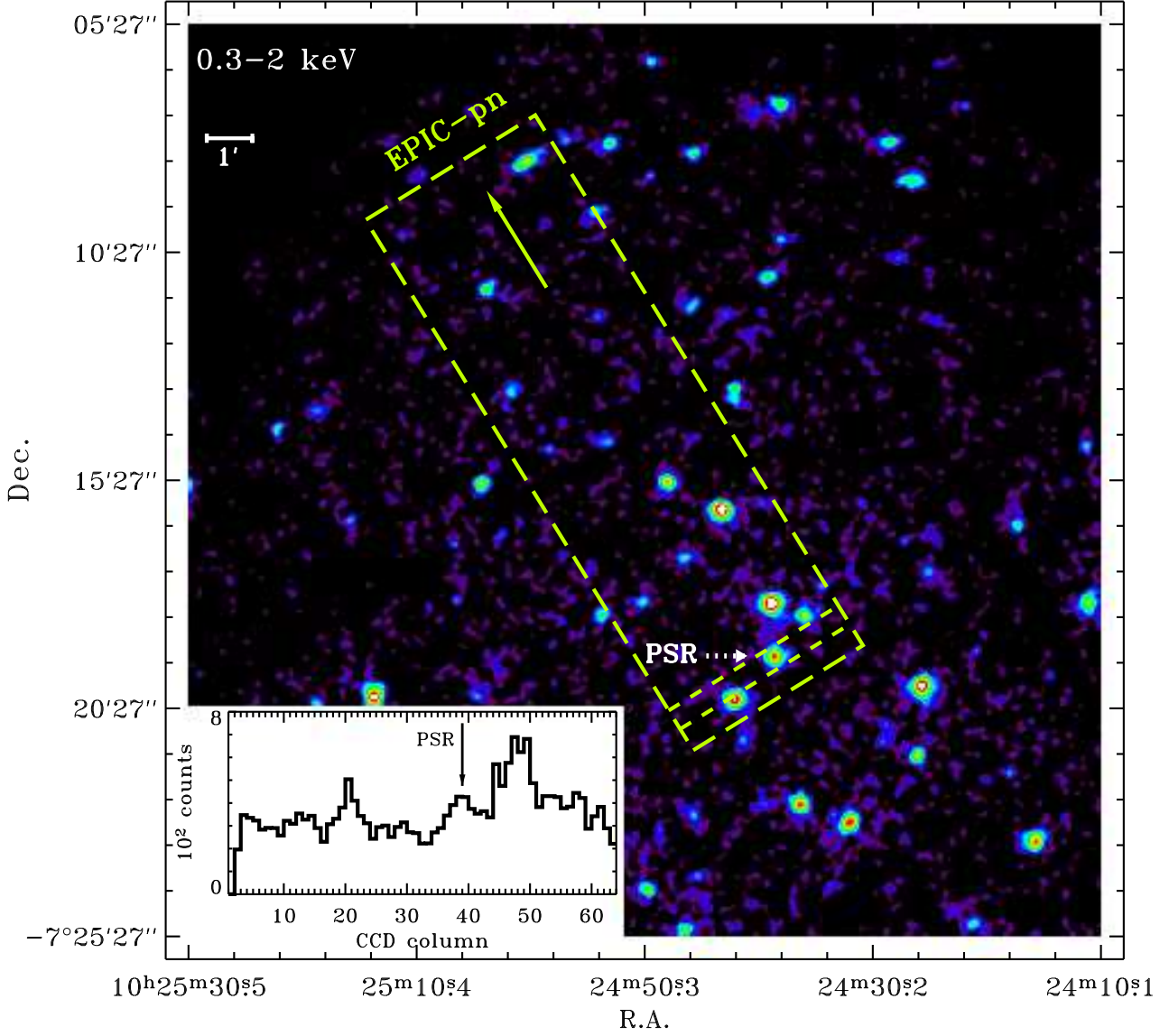


Fig. 10.— Combined EPIC-MOS1 and MOS2 image in the 0.3–5 keV range, with PSR J1024–0719 indicated with dotted arrow (see caption to Fig. 1 for other details). Emission of the pulsar dominates in the area between two short-dashed lines within the EPIC-pn field of view. One-dimensional distribution of EPIC-pn counts is shown in the insert.

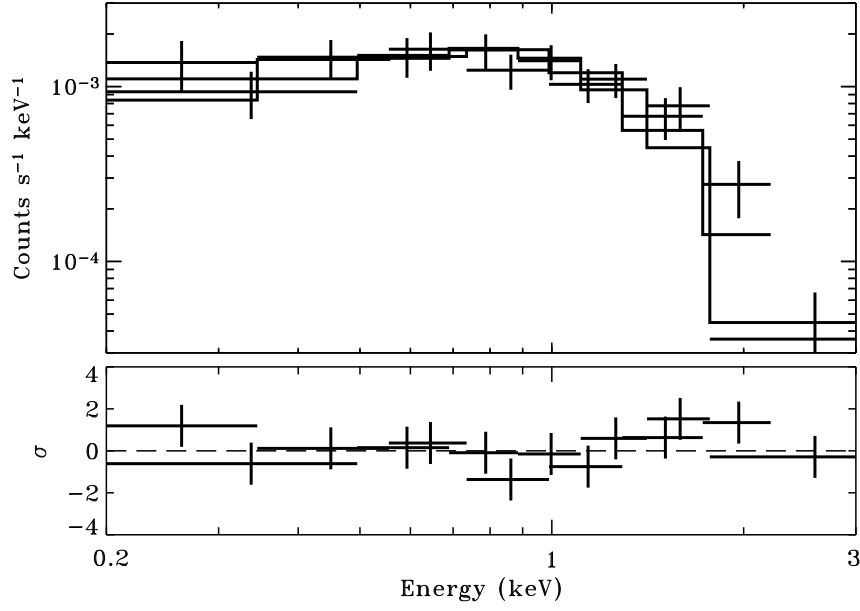


Fig. 11.— Two EPIC-MOS phase-integrated spectra of PSR J1024–0719 fitted with a polar cap model, and residuals of the fit.

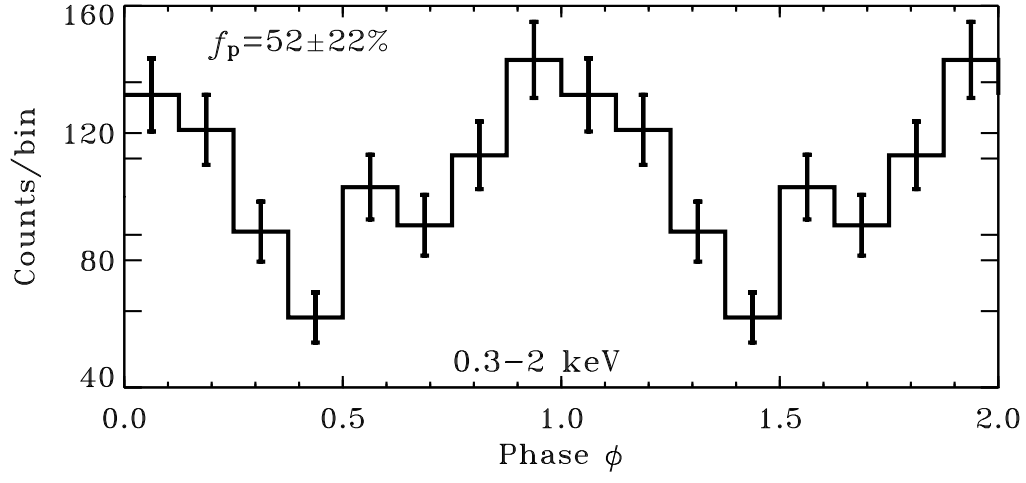


Fig. 12.— Pulse profile of PSR J1024–0719 extracted from the EPIC-pn data in the 0.3–2 keV range, with estimated value of the intrinsic source pulsed fraction  $f_p$ .



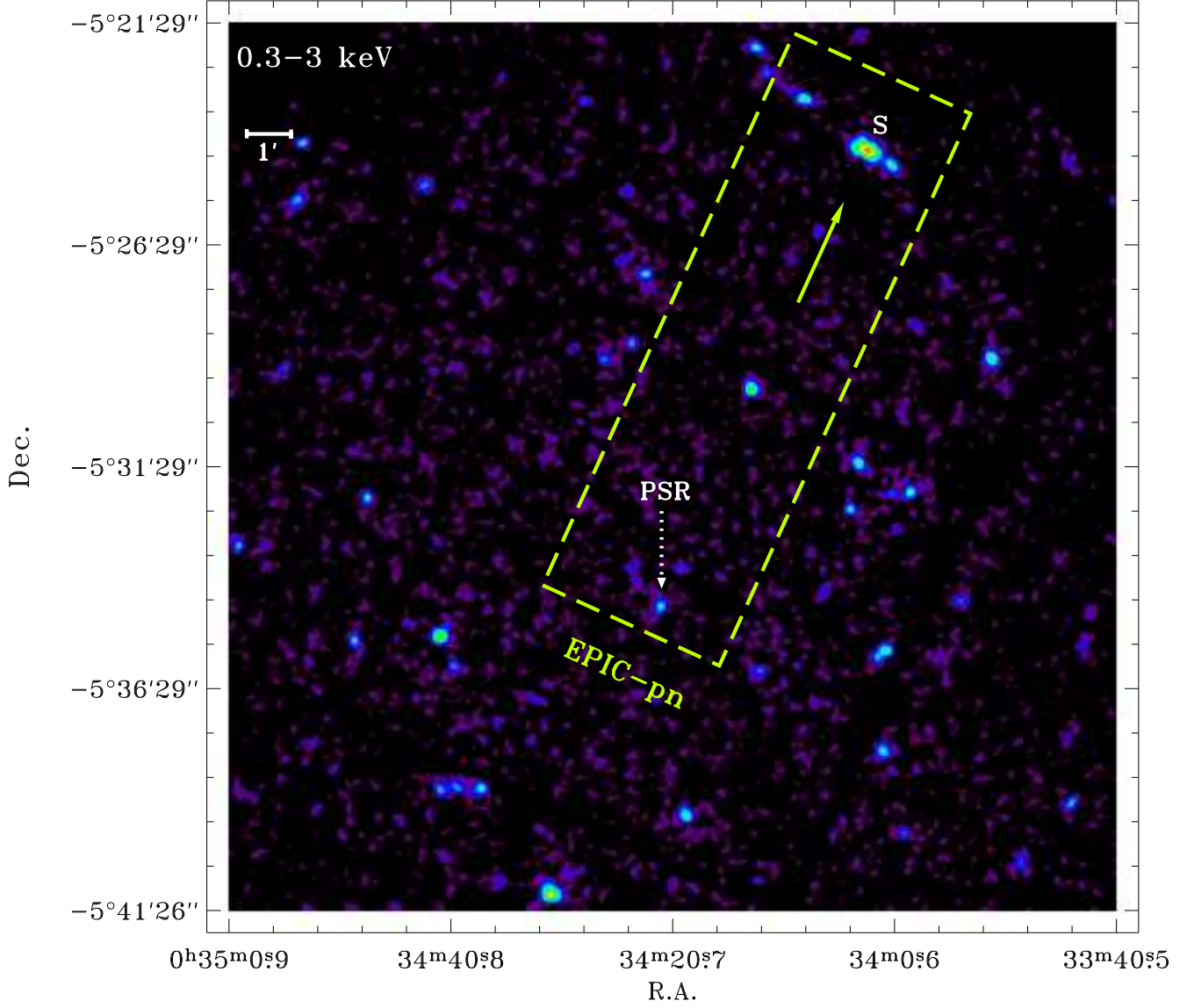


Fig. 13.— Combined EPIC-MOS1 and MOS2 image in the 0.3–3 keV range, with PSR J0034–0534 indicated with dotted arrow (see caption to Fig. 1 for other details). The brightest source in the filed of view is marked with the label “S”.